RSC Advances

PAPER

View Article Online
View Journal | View Issue



Cite this: *RSC Adv.*, 2019, **9**, 24291

# Ferroelectric properties and Raman spectroscopy of the $[(C_4H_9)_4N]_3Bi_2Cl_9$ compound†

W. Trigui * and F. Hlel

Received 5th April 2019
Accepted 24th July 2019

DOI: 10.1039/c9ra02577d

rsc.li/rsc-advances

The exploration of ferroelectric hybrid materials is highly appealing due to their great technological significance. They have the potential to conserve power and amazing applications in information technology. In line with this, we herein report the development of a $[(C_4H_9)_4N]_3Bi_2Cl_9$ tetra-alkyl hybrid compound that exhibits ferroelectric properties. The phase purity was confirmed by Rietveld refinement of the X-ray powder diffraction pattern. It crystallizes, at room temperature, in the monoclinic system with the $P2_1/n$ space group. The outcome of temperature dependence of the dielectric constant proved that this compound is ferroelectric below approximately 238 K. The dielectric constants have been fitted using the modified Curie–Weiss law and the estimated $\gamma$ values are close to 1. This confirms classical ferroelectric behavior. Raman spectroscopy is efficiently utilized to manifest the origin of the ferroelectricity, which is ascribed to the dynamic motion of cations as well as distortion of the anions. Moreover, the analysis of the wavenumbers and the half-width for $\delta_s$(Cl–Bi–Cl) and $\omega(CH_2)$ modes, based on the order–disorder model, allowed us to obtain the thermal coefficient and activation energy near the para-ferroelectric phase transition.



## 1. Introduction

The design of organic–inorganic hybrid materials, based on trivalent metal halides, has attracted scientific attention not only due to their interesting structural diversity but also to their unique physical properties as well as possible novel applications in optoelectronics, photovoltaic cells, semiconductor devices, electrochemical transistors, and electroluminescent diodes.[1–4]

Crystals of halogeno-bismuthates(III) and antimonates(III) with tetralkylammonium cations with the general formula $[(C_nH_{2n+1})_4N]_3M_2X_9$ (where $[(C_nH_{2n+1})_4N]$ = organic cations with $n$ = 1, 2, 3 or 4; M = Bi, Sb and X = Cl, Br, I) are frequently characterized by their phase transitions.[5–8] It was found that the complexity of the phase transitions increases with increasing the "$n$" number of carbon atoms in the alkylammonium chain up to four carbon atoms.[9,10]

The phase transitions are usually connected with an appearance of interesting physical properties such as ferroelectricity and ferroelasticity, *etc*.[11–13] Thus, the para-ferroelectric phase transitions are characterized by an "order–disorder" mechanism related to the dynamical reorientation of the alkyl cation's chains.[14–17] This motion is substantially diminished on lowering temperature yielding ordered phases.[18]

The anionic $[M_2X_9]^{3-}$ sublattices are built of basic distorted $MX_6$ octahedral units sharing corners, edges or faces to form anionic discrete bioctahedra (0D),[19] chains (1D)[20] or layers (2D).[21] It is worthwhile to mention that a special interest has been focused on compounds with the inorganic halide $M_2X_9$ since the discovery of their ferroelectric properties.[22,23]

In this work we intend to spot on the nature of para-ferroelectric phase transition at 238 K in $[(C_4H_9)_4N]_3Bi_2Cl_9$ compound. The crystal structure of this hybrid compound, at room temperature, was previously determined and reported.[24]

In this contribution, we report the results of the X-ray powder diffraction, dielectric and Raman studies. The temperature dependence of Raman spectra have enabled us to establish the key role played by the tetra-butylammonium cations and the halogeno-bismuthate anions, in the para-ferroelectric transition.

## 2. Experiments and methods

Phase purity, space group and lattice parameters were checked by X-ray powder diffraction analysis. XRD data was collected, at room temperature, using a Philips PANalytical X'pert Pro X-ray powder diffractometer operating with copper radiation ($\lambda$ = 1.540598 Å) over a wide range of Bragg angles ($6° \leq 2\theta \leq 52°$). Refinements were carried out using FULLPROF program based on Rietveld method.[25]

The impedance analyzer (Agilent 4294A) was used to characterize the dielectric properties in the frequency range, between 50 Hz and 6 MHz, in the temperature range within

*Faculty of Sciences, Laboratory of Spectroscopic and Optical Characterization of Materials, University of Sfax, BP1171, 3018 Sfax, Tunisia*

† Electronic supplementary information (ESI) available. See DOI: 10.1039/c9ra02577d

195–260 K. The polycrystalline material was used in a form of a pressed pellet with a diameter equal to 8 mm and a thickness of 1.3 mm.

Raman spectra of $[(C_4H_9)_4N]_3Bi_2Cl_9$ monocrystalline sample were collected using a T-64000 Raman (Horiba-Jobin-Yvon) with cooled CCD detector. The excitation wave-length radiation was 647.1 nm, using an argon-krypton laser (coherent spectrum) with a 50 mW power. The spectra were registered with 1800 per mm grating from 170 to 3300 $cm^{-1}$. The resolution of the instrument was set at 0.2 $cm^{-1}$. The measurements were carried out under microscope in the backscattering geometry using an X-50 LF objective, on the (001) natural face of single crystal in $Z(XX)Z$ polarization, where $X$ stands for a birefringence direction. The low temperature measurements were performed with a cold liquid nitrogen cryostat. Temperature stability around ±1 K was achieved. The error range for the determination of the peak position was ±0.3 $cm^{-1}$.

# 3. Results and discussion

## 3.1. X-ray powder diffraction analysis

The X-ray diffraction pattern at 293 K for the tri-tetrabutylammonium nona chlorobibismuthate ($TBA_3Bi_2Cl_9$) compound is plotted in Fig. 1. The circles symbolize the experimental data and the line corresponds to the simulated pattern. The green bars indicate good matching of all the peak positions.

The purity of the studied compound was proved and all reflection peaks are successfully refined in the monoclinic system with $P2_1/n$ space group, using Rietveld method. The corresponding lattice parameters were found to be: $a = 11.356$ Å, $b = 22.342$ Å, $c = 28.587$ Å, $\beta = 96.59°$ and the cell volume was $V = 7155.32$ Å$^3$. Those parameters are in good agreement with the published results.[24] The quality of the refinement was evaluated through the goodness of fit $\chi^2 = 1.20$ and the reliability factors obtained are $R_{\omega p} = 11.90$, $R_p = 11.80$ and $R_{exp} = 10.85$.

## 3.2. Dielectric studies

The temperature dependence of the real part $\varepsilon'$, imaginary part $\varepsilon''$of the dielectric permittivity and the dielectric loss $T_g(\delta)$, of different frequencies, are plotted in Fig. 2. From these curves, we can observe two dielectric relaxations around 214 and 235 K in the $\varepsilon'$ variation but only one relaxation in the $\varepsilon''$ and $T_g(\delta)$ plots ($T_c = 235$ K). This prominent dielectric peak at $T_c$ may be associated to a para-ferroelectric phase transition in the title compound. Its maximum does not change while the magnitude decreases with the increase in frequency. In fact, this result suggests that this sample does not present any type of dielectric relaxation in the investigated frequency range.[26,27]

The dielectric data in the paraelectric state obey quite well the Curie–Weiss law, described by the following relation:

$$\varepsilon' = \frac{C}{T - T_0} \quad (1)$$

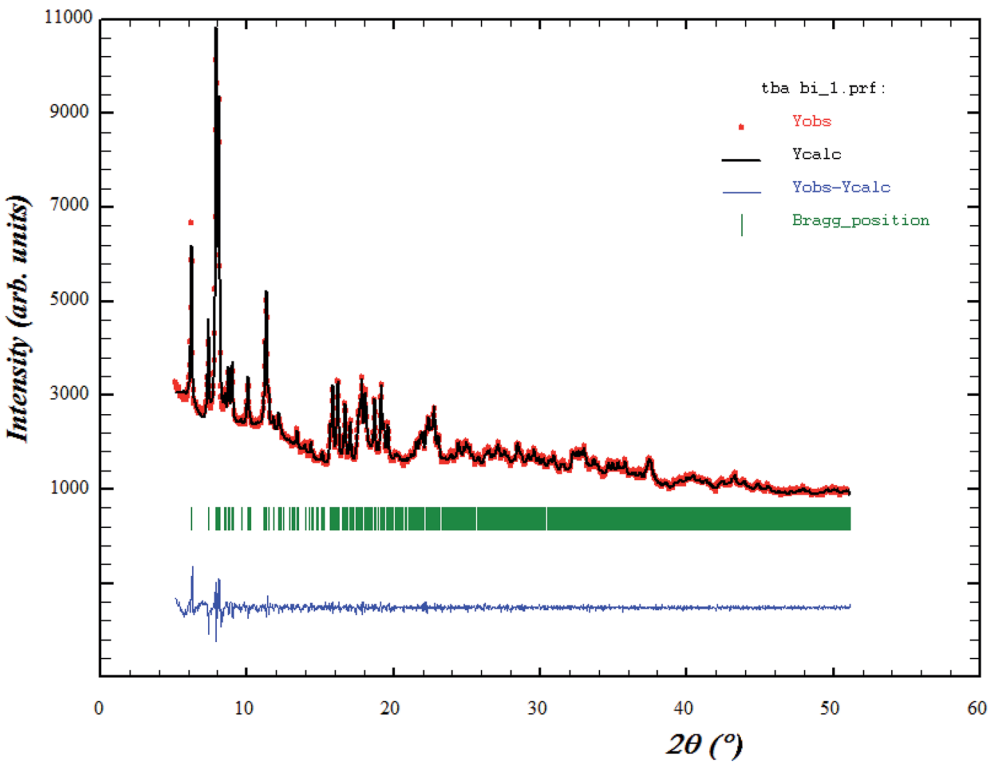


Fig. 1 Plot of the Rietveld refinement at room temperature of $[(C_4H_9)_4N]_3Bi_2Cl_9$ compound. The red dots indicate the experimental data and the black continuous line represent the calculated pattern. The green vertical bars describe the Bragg position.

 

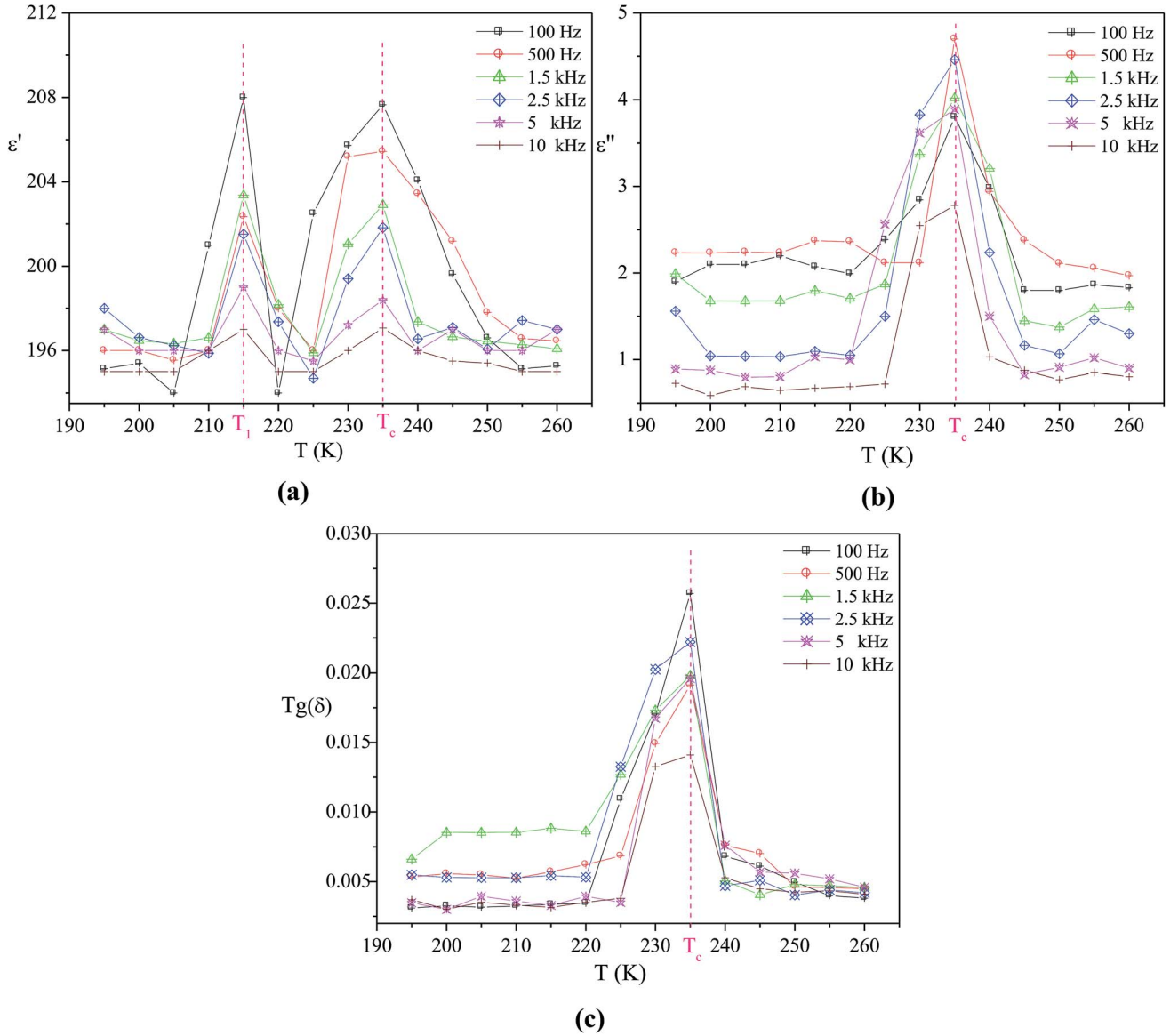


Fig. 2 Temperature dependence at various frequencies of the real part $\varepsilon'$ of the complex permittivity (a), the imaginary part $\varepsilon''$ of the complex permittivity (b) and the dielectric loss $T_g(\delta)$ (c).

where $C$ and $T_0$ are the Curie–Weiss constant and temperature, respectively.

The temperature dependence of the dielectric reciprocal ($1/\varepsilon'$), at 500 Hz, is illustrated in Fig. 3a. This plot gives a straight line with the $X$-axis intercept at $T_0 = 227$ K. For the classical ferroelectrics, the order of the para-ferroelectric phase transition can be determined from the value of $T_0$. In case of $T_0 \neq T_C$, the phase transition is of a first order type. If $T_0 = T_C$, this transition is of a second order type.[28] According to our measurements, the value of $T_0$ is different from $T_C = 235$ K which suggests that this transition is of the first order type[29,30] and confirms the drawing results from the differential scanning calorimetry analysis.[24]

In order to determine the nature of classic or relaxor ferroelectrics, Uchino and Nomura[31] have proposed a more general expression of the Curie–Weiss law by introducing the exhibitor criticizes $\gamma$:

$$\frac{1}{\varepsilon'} - \frac{1}{\varepsilon'_{max}} = \frac{(T - T_C)^{\gamma}}{C} \quad (2)$$

where $C$ is the Curie–Weiss constant, $\varepsilon'_{max}$ is the real dielectric constant at $T = T_C$ and $\gamma$ ($1 < \gamma < 2$) corresponds to the degree of relaxation.

The factor $\gamma$ translates the diffuse character of the transition. However, for ideal relaxor ferroelectrics, the $\gamma$ value should amount to 2, and for classical ferroelectrics it is near to 1.[32,33]

Fig. 3b shows the logarithmic plots related to the eqn (2) at various frequencies. The obtained $\gamma$ values are 1.152, 1.286 and 1.008 corresponding to the frequencies 100 Hz, 2.5 kHz and 10 kHz, respectively. This result proves that the $[(C_4H_9)_4N]_3Bi_2Cl_9$ is a classical ferroelectric compound.

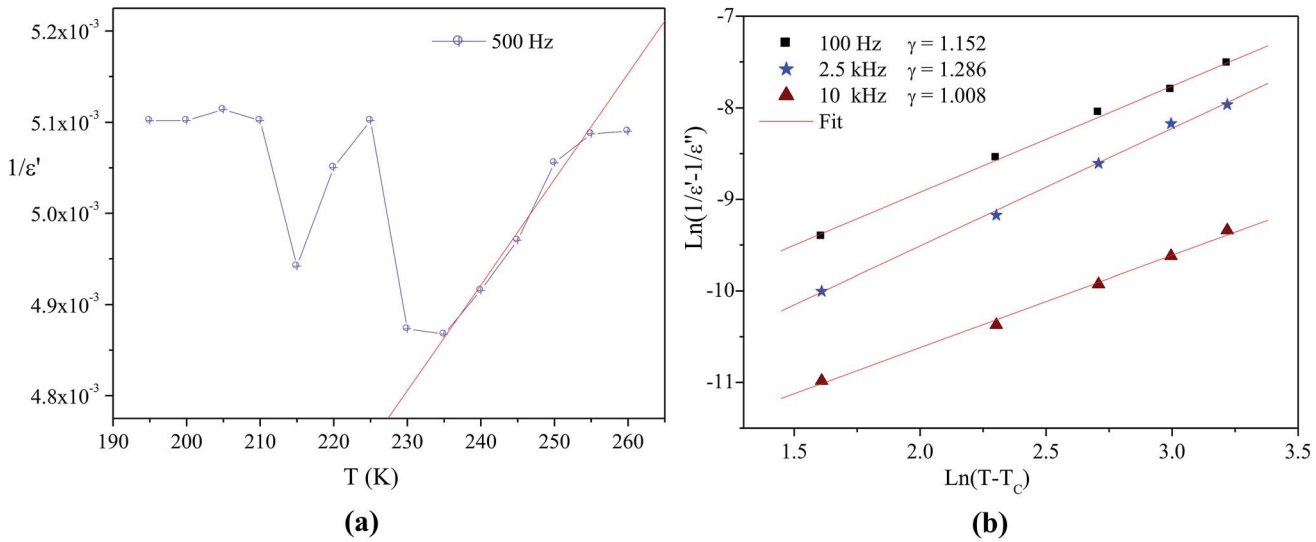


Fig. 3 (a) Temperature variation of $1/\varepsilon'$ at some frequency, (b) $\ln(1/\varepsilon' - 1/\varepsilon'_{max})$ as a function of $\ln(T - T_C)$ for different frequency (the solid red lines denote the fitting curve to the modified Curie–Weiss law).

### 3.3. Temperature evolution of the Raman spectra

The assignment of the Raman spectrum at room temperature has been performed and presented in table S. Raman spectra in the frequency range 170–3300 $cm^{-1}$, have been collected for several temperatures (from 193 to 258 K). Fig. 4 shows the temperature evolution of Raman spectra obtained in three spectral ranges.

The positions of most analyzed bands are constant even in the close vicinity of both phase transitions. However, one can distinguish several bands showing changes in their positions and width at half maximum, by the order of a few $cm^{-1}$ when crystal undergoes the phase transitions at $T_1$ and $T_2$.

In order to quantitatively analyze the evolution of Raman bands *versus* temperature, each spectrum were analyzed by means Labspec software on the basis of Gaussian and Lorentzian shapes. Fig. S1 and S2† reports position and half-width temperature dependence of selected lines, respectively.

The lines issued from the internal modes of $Bi_2Cl_9$ anions do not show significant changes where the wavenumbers and lines width exhibit a slight change. However, the Cl–Bi–Cl bending vibration at 184.4 $cm^{-1}$, presents a remarkable shift toward high frequencies (of 3 $cm^{-1}$) and a line broadening (of 5 $cm^{-1}$) on heating above the phase transitions.

We may say that the increase of dynamical motion of the alkyl chains of tetrabutylammonium cations has evoked the distortion of the bi-octahedral anions.[5,34]

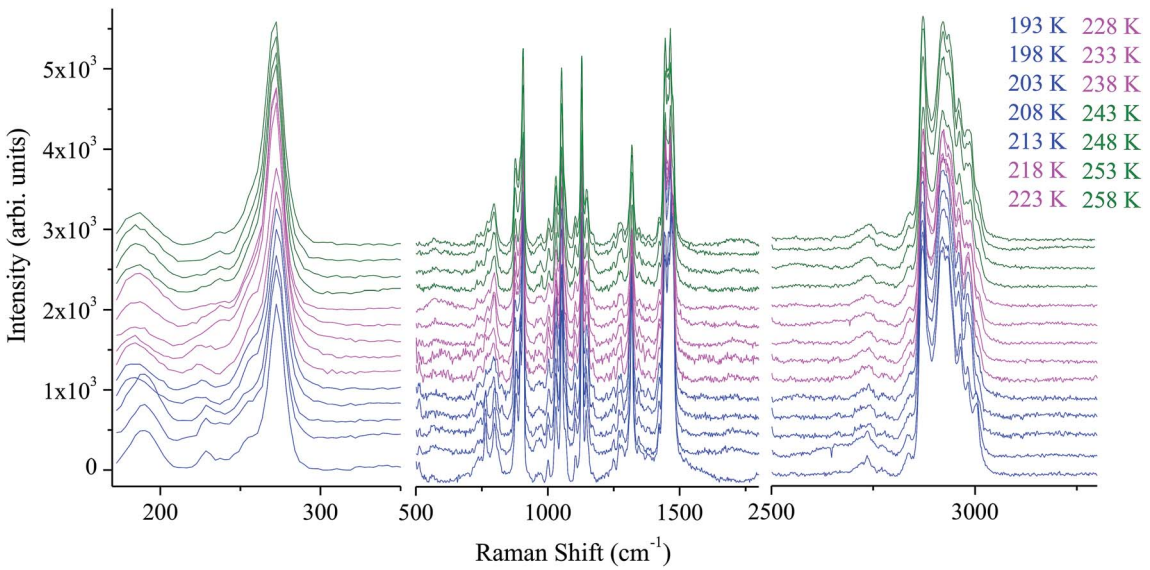


Fig. 4 Temperature evolution of the Raman spectra for selected spectral ranges.

The band related to the symmetric stretching vibration $\nu_s$(C–C) is located at 797.4 $cm^{-1}$. Its maximum shifts toward lower wavenumbers by 3 $cm^{-1}$ around $T_1$ and towards higher wavenumbers around $T_2$. A similar behavior was observed for the band located at 769.8 $cm^{-1}$ which is assigned to $\nu_4(NC_4)$ and $\rho_r(CH_2)$. The symmetric stretching vibration $\nu_s$ of $(CH_2)$ and $(CH_3)$ groups shows a variation in its position to the high frequencies by 3 $cm^{-1}$ and by 5 $cm^{-1}$ in its half-width. The band at 1319.8 $cm^{-1}$ assigned to the wagging mode of $(CH_2)$ group increase by 3 $cm^{-1}$, while the variation of the symmetric bending vibration $\delta_s$(C–C–C) and $\delta_s$(C–N–C) observed at 906.9 $cm^{-1}$ is by 2 $cm^{-1}$ for both wavenumber and half-width.

Over the phase I, the band corresponding to the antisymmetric bending mode $\delta_{as}(CH_3)$ weakly moves to high frequencies. To verify that the phase transitions are connected to a change in the dynamical state of the $[(C_4H_9)_4N]^+$ cations and to the distortion of the $[Bi_2Cl_9]^{3-}$ anions, we have focused our study on tow selected bands P2 and P29 associated to the bending vibration of (Cl–Bi–Cl) and to the wagging mode $\omega(CH_2)$ (Fig. 5), respectively.

**3.3.1. Temperature dependence of the wavenumber.** The temperature dependence of Raman wavenumber, of a phonon connected to an order–disorder mechanism, according to Andrade and Porto[35,36] can be described by:

$$\nu^2 = \nu_0{}^2\left[1 + \gamma\left(T - T_j\right)\right] \quad (3)$$

where $\gamma$ is the thermal coefficient, $T_j$ is the temperature of phase transition $j$, $\nu_0$ is the hard-core wavenumber at transition temperature.

Generally, the values of $\gamma$ are small so that we can approximate eqn (3) by:

$$\nu = \nu_0\left[1 + \frac{\gamma}{2}\left(T - T_j\right)\right] \quad (4)$$

The experimental values of $P_2$ and $P_{29}$ modes wavenumber, at various temperatures, were fitted to the equation above (Fig. 6a and b). A summary of the experimental thermal coefficient $\gamma$ values are collected in Table 1. The "hard-core" frequency $\nu_0$ values, for the two bands, are (182.7, 1316.5 $cm^{-1}$) at $T_1$ and (185.8, 1319.1 $cm^{-1}$) at $T_2$, respectively.

The thermal coefficient is related to the variation of the wavenumber position and the volume of the crystal. It is expressed by the following equation:

$$\gamma_i = -\frac{\Delta\nu_i}{\nu_i} \times \frac{V}{\Delta V} \quad (5)$$

where $\Delta V$ is the volume, $\Delta\nu_i$ is the variation of the wavenumber position, $V$ symbolizes the original volume and $\nu_i$ the band position of the i mode at room temperature.

According to Gruneisen,[37] the relative change of each vibrational frequency is directly proportional to the relative change in the volume. The increase of the thermal coefficient, related to the shift of the two peaks positions to high frequencies, indicates a decrease of the crystal volume.[38] Indeed, the cation geometry can be changed from cross symmetry to broken cross symmetry by reorientational motion of the alkylammonium chains going through the phase transitions.[16,39] This behavior suggests that the observed phase transitions are related to the reorientational motion of the cations coupled to the distortion of the anions.

**3.3.2. Temperature dependence of the full width at half maximum.** We performed a detailed analysis of the bands shape for Cl–Bi–Cl bending and wagging mode of the $(CH_2)$ group. It was shown that the temperature dependence of the full-width at the half-maximum (FWHM) fulfils the Carabatos-Nédelec and Becker model.[40] This model is based on the damping theory of the oscillation associated with an order–disorder mechanism in the solid state.[41]

According to Langevin[42,43] the temperature dependence of FWHM can be expressed as:

$$\tau = a + bT + c\frac{\tau_R}{1 + \omega^2{\tau_R}^2} \quad (6)$$

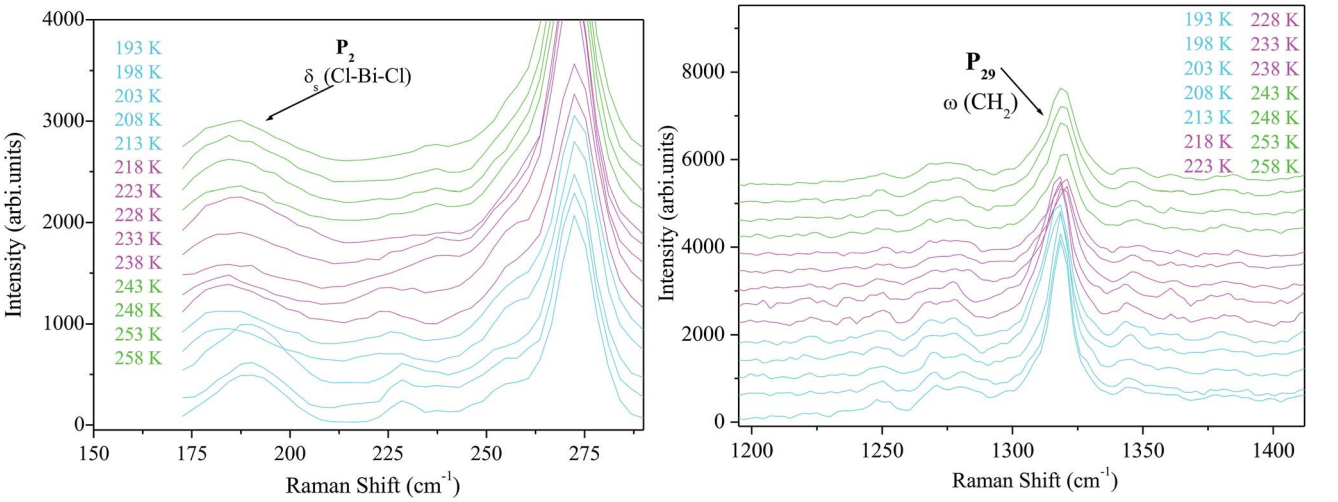


Fig. 5 Temperature evolution of the Raman spectra in the frequency region assigned to the bending vibration of (Cl–Bi–Cl) and to the wagging mode of $(CH_2)$.

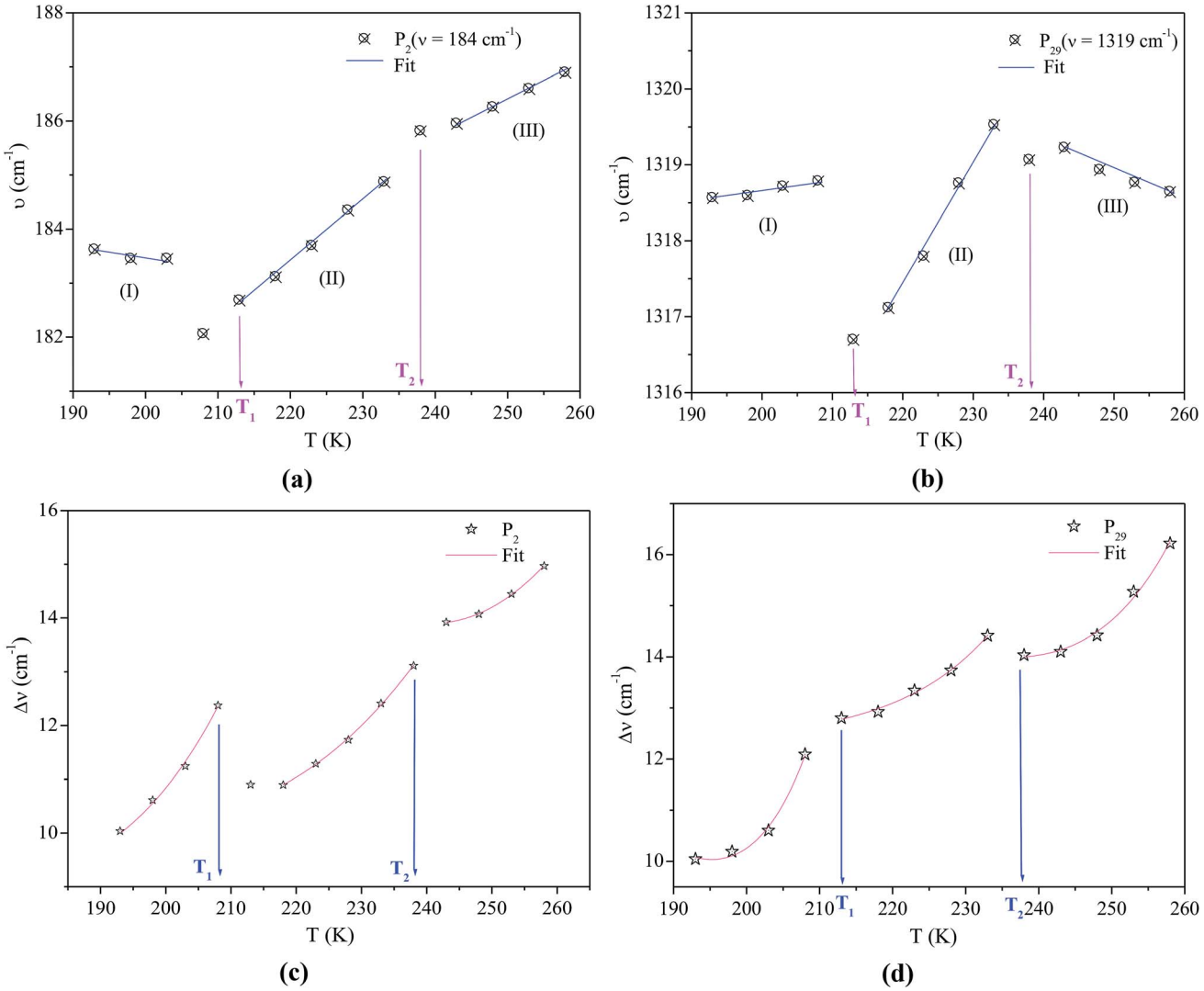


Fig. 6 (a and b) Raman wavenumbers *versus* temperature of the bands $P_2$ and $P_{29}$, (c and d) line width *versus* temperature of the bands $P_2$ and $P_{29}$ (the red line is the fit to the Carabatos-Nédelec and Becker model).

Table 1 Thermal coefficients of the wavenumber variation *vs.* temperature of the peaks $P_2$ and $P_{29}$

| Peak | Temperature range | Thermal coefficient, $\gamma$ ($K^{-1}$) |
|---|---|---|
| $P_2$ | $T < T_1$ | $\gamma = -1.83 \times 10^{-4}$ |
| | $T_1 < T < T_2$ | $\gamma = 1.23 \times 10^{-3}$ |
| | $T > T_2$ | $\gamma = 6.83 \times 10^{-4}$ |
| $P_{29}$ | $T < T_1$ | $\gamma = -2.48 \times 10^{-5}$ |
| | $T_1 < T < T_2$ | $\gamma = 2.49 \times 10^{-4}$ |
| | $T > T_2$ | $\gamma = 5.97 \times 10^{-5}$ |

where $(\omega\tau_R)^2 \gg 1$, $\omega = 2\pi\nu$ is the phonon wavenumber and $\tau_R$ is the mean reorientational time of the atoms to jump from one potential well to another.

The mean reorientational time of the atoms $\tau_R$ is given by:

$$\tau_R = \tau_\infty \exp\left(\frac{E_a}{RT}\right) \quad (7)$$

where $\tau_\infty$ is the relaxation time at infinite temperature, $E_a$ is the activation energy for the mode connected to the order–disorder transition and $R$ (=8.314472 J $K^{-1}$ $mol^{-1}$) is the perfect gas constant. Therefore the eqn (6) can be written as:[44]

$$\mathrm{FWHM}(T) = (a + bT) + c \exp\left(-\frac{E_a}{RT}\right) \quad (8)$$

where $a$, $b$, c and $E_a$ are the fitting parameters. $E_a$ is the activation energy of the reorientation process. The linear part of eqn (8) corresponds to the vibrational relaxation and the exponential term, related to the thermal molecular motions, corresponds to the reorientational relaxation.

The values of the full widths at half maximum are obtained using ultra-high resolution triple additive configuration. Fig. 6c and d show the FWHM experimental values of $P_2$ and $P_{29}$, at various temperatures, fitted according to eqn (8).

For the bending vibration of (Cl–Bi–Cl), the estimated activation energy values are $E_a(I) = 18.23$ kJ $mol^{-1}$ for $T < T_1$, $E_a(II) =$

 

15.59 kJ mol$^{-1}$ for $T_1 < T < T_2$ and $E_a$(III) = 11.46 kJ mol$^{-1}$ for $T > T_2$. Whereas, the obtained values for the wagging mode $\omega(CH_2)$ are $E_a$(I) = 40.60 kJ mol$^{-1}$ for $T < T_1$, $E_a$(II) = 35.92 kJ mol$^{-1}$ for $T_1 < T < T_2$ and $E_a$(III) = 30.96 kJ mol$^{-1}$ for $T > T_2$. In fact, the decrease in activation energy values for these Raman bands is probably due to the decrease in the population involved in these vibrations, which may be related to the change of the $[(C_4H_9)_4N]^+$ cations conformation as well as the distortion of the $[Bi_2Cl_9]^{3-}$ anions.

## 4. Conclusion

The $[(C_4H_9)_4N]_3Bi_2Cl_9$ compound, with $P2_1/n$ space group of the monoclinic system was investigated as a function of temperature. The existence of a para-ferroelectric phase transition at 238 K has been established by the dielectric measurements. The empirical parameter $\gamma$ indicates that this compound is a classical ferroelectric. The Raman spectroscopic study clearly shows spectacular temperature changes of the internal vibrations of cation and the anion, especially the deformation of (Cl–Bi–Cl) and the ($CH_2$) wagging mode. A detailed analysis of the wavenumber and the bandwidth was performed in the framework of order–disorder models. This study proves that the phase transitions are related to the rotational motion of the tetrabutylammonium cations and to the distortion of the $[Bi_2Cl_9]^{3-}$ anions.

## Conflicts of interest

There are no conflicts to declare.

## References

1 R. Jakubas and L. Sobczyk, Phase transitions in alkylammonium halogenoantimonates and bismuthates, *Phase Transitions*, 1990, **20**, 163–193.
2 S. T. Han, Y. Zhou and V. A. Roy, Towards the Development of Flexible Non-Volatile Memories, *Adv. Mater.*, 2013, **25**, 5425–5449.
3 I. Matulková, J. Cihelka, M. Pojarová, K. Fejfarova, M. Dušek, P. Vanek, J. Kroupa, R. Krupková, J. Fábry and I. Nemec, A new series of 3,5-diamino-1,2,4-triazolium(1+) inorganic salts and their potential in crystal engineering of novel NLO materials, *CrystEngComm*, 2012, **14**, 4625–4636.
4 C. Sanchez, B. Julian, P. Belleville and M. Popall, Applications of hybrid organic–inorganic nanocomposites, *J. Mater. Chem.*, 2005, **15**, 3559–3592.
5 W. Trigui, A. Oueslati, F. Hlel and A. Bulou, Raman study of order–disorder phase transition in $[(C_3H_7)_4N]_3Bi_3Cl_{12}$ compound, *J. Mol. Struct.*, 2016, **1106**, 19–29.
6 S. Hajlaoui, I. Chaabane, A. Oueslati, K. Guidara and A. Bulou, Raman scattering investigation of the high temperature phase transition in $[N(C_3H_7)_4]_2SnCl_6$, *Spectrochim. Acta, Part A*, 2015, **136**, 547–552.
7 N. Weslati, I. Chaabane and F. Hlel, A theoretical study on the molecular structure and vibrational (FT-IR and Raman) spectra of a new organic–inorganic compound of 2 $[N(C_3H_7)_4]SbCl_4$, *Vib. Spectrosc.*, 2015, **81**, 90–95.
8 G. Bator, R. Jakubas and J. Baran, Vibrational study of the structural phase transitions in the $(CH_3ND_3)_3Sb_2Br_9$ (d-MABA) crystals by infrared spectroscopy, *Vib. Spectrosc.*, 2001, **25**, 101–113.
9 I. Płowaś, A. Białońska, G. Bator, R. Jakubas, W. Medycki and J. Baran, Tris(allylammonium) Hexabromobismuthate(III)-Crystal Structure, Phase Transitions and Thermal, Dielectric, Vibrational and $^1$H NMR Properties Over a Range of Temperatures, *Eur. J. Inorg. Chem.*, 2012, **4**, 636–646.
10 J. Tarasiewicz, R. Jakubas, J. Zaleski and J. Baran, Structural characterization, thermal, dielectric and spectroscopic properties of di(*n*-pentylammonium) pentabromoantimonate(III): $[n\text{-}C_5H_{11}NH_3]_2[SbBr_5]$, *J. Mol. Struct.*, 2008, **876**, 86–101.
11 M. Ben Bechir, K. Karoui, M. Tabellout, K. Guidara and A. Ben Rhaiem, Electric and dielectric studies of the $[N(CH_3)_3H]_2CuCl_4$ compound at low temperature, *J. Alloys Compd.*, 2014, **588**, 551–557.
12 R. Jakubas, J. Jóźków, G. Bator, J. Zaleski, J. Baran and P. Frangois, Phase transitions in *i*-butylammonium halogenoantimonate(III) and bismuthate(III) crystals, *J. Mol. Struct.*, 1997, **436**, 315–325.
13 Y. Heng-Yun, T. Yuan-Yuan, L. Peng-Fei, L. Wei-Qiang, G. Ji-Xing, H. Xiu-Ni, C. Hu, S. Ping-Ping, Y. Yu-Meng and X. Ren-Gen, Metal-free three-dimensional perovskite ferroelectrics, *Science*, 2018, **361**, 151–155.
14 J. Tarasiewicz, R. Jakubas, J. Baran and A. Pietraszko, On the structural phase transitions in $[n\text{-}C_4H_9NH_3]_2[SbBr_5]$: thermal, dielectric and infrared studies, *J. Mol. Struct.*, 2004, **697**, 161–171.
15 H. Chouaib, N. Elfaleh, S. Karoui, S. Kamoun and M. P. F. Graça, Synthesis, crystal structure, thermal analysis and dielectric properties of $(C_8H_{12}N)_3SnCl_6Cl$ compound, *Synth. Met.*, 2016, **217**, 129–137.
16 J. Binns, G. J. McIntyre, J. A. Barreda-Argueso, J. Gonzalez, F. Aguado, F. Rodriguez, R. Valiente and S. Parsons, Phase transition sequences in tetramethylammonium tetrachlorometallates by X-ray diffraction and spectroscopic measurements, *Acta Crystallogr., Sect. B: Struct. Sci., Cryst. Eng. Mater.*, 2017, **73**, 844–855.
17 A. R. Lim and K. Y. Lim, Structural changes near phase transition temperatures for the $[N(C_2H_5)_4]$ groups in hydrated $[N(C_2H_5)_4]_2CuCl_4xH_2O$, *J. Therm. Anal. Calorim.*, 2017, **130**, 879–884.
18 B. Zarychta and J. Zaleski, Phase Transitions Mechanism and Distortion of $SbCl_6^{3-}$ Octahedra in Bis(*n*-butylammonium) Pentachloroantimonate(III) $(C_4H_9NH_3)_2[SbCl_5]$, *Z. Naturforsch., B: J. Chem. Sci.*, 2006, **61**, 1101–1109.
19 D. Fredj, C. Ben Hassen, S. Elleuch, H. Feki, N. C. Boudjada, T. Mhiri and M. Boujelbene, Structural, vibrational and optical properties of a new organic–inorganic material: $(C_5H_8N_3)_2[BiCl_5]$, *Mater. Res. Bull.*, 2017, **85**, 23–29.

20 N. A. Yelovik, A. V. Mironov, M. A. Bykov, A. N. Kuznetsov, A. V. Grigorieva, Z. Wei, E. V. Dikarev and A. V. Shevelkov, Iodobismuthates Containing One-Dimensional $BiI_4^-$ Anions as Prospective Light-Harvesting Materials: Synthesis, Crystal and Electronic Structure, and Optical Properties, *Inorg. Chem.*, 2016, **55**, 4132–4140.

21 S. A. Adonin, M. N. Sokolov and V. P. Fedin, Polynuclear halide complexes of Bi(III): From structural diversity to the new properties, *Coord. Chem. Rev.*, 2016, **312**, 1–21.

22 P. Szklarz, R. Jakubas, A. Piecha-Bisiorek, G. Bator, M. Chański, W. Medycki and J. Wuttke, Organic–inorganic hybrid crystals, 2,4,6-$CH_3PyH_3Sb_2Cl_9$ and 2,4,6-$CH_3PyH_3Bi_2Cl_9$. Crystal structure characterization and tunneling of $CH_3$ groups studied by $^1H$ NMR and neutron spectroscopy, *Polyhedron*, 2018, **139**, 249–256.

23 B. Kulicka, T. Lis, V. Kinzhybalo, R. Jakubas and A. Piecha, Novel anionic water-containing inorganic fragment in [4-$NH_2PyH]_8[Bi_2Cl_{11}][Bi_2Cl_9(H_2O)_2]$: Structural characterization, thermal, dielectric and vibrational properties, *Polyhedron*, 2010, **29**, 2014–2022.

24 W. Trigui, A. Oueslati, I. Chaabane and F. Hlel, Synthesis, crystal structure, thermal analysis and dielectric properties of $[(C_4H_9)_4N]_3Bi_2Cl_9$ compound, *J. Solid State Chem.*, 2015, **227**, 10–16.

25 J. Rodriguez-Carvajal, Recent advances in magnetic structure determination by neutron powder diffraction, *Phys. B*, 1993, **192**, 55–69.

26 H. Khemakhem, T. Mhiri and A. Daoud, Ferroelectric and electric properties of $Rb_{0.6}(NH_4)_{0.4}HSO_4$ single crystal, *Solid State Ionics*, 1999, **117**, 337–343.

27 R. M. Shymkiv, S. A. Svelber, I. V. Karpa, I. N. Katerynchuk, I. M. Kunyo and E. I. Phitsych, Electronic spectra and phase transitions in thin $[N(CH_3)_4]_2CuCl_4$ microcrystals, *Appl. Spectrosc.*, 2012, **78**, 823–828.

28 A. Rhaiem, F. Jomni, K. Karoui and K. Guidara, Ferroelectric properties of the $[N(CH_3)_4]_2CoCl_2Br_2$ compound, *J. Mol. Struct.*, 2013, **1035**, 140–144.

29 R. Hajji, A. Oueslati, F. Hajlaoui, A. Bulou and F. Hlel, Structural characterization, thermal, ac conductivity and dielectric properties of $(C_7H_{12}N_2)(2)$ $SnCl_6$ Cl-2 center dot $1.5H_2O$, *Phase Transitions*, 2016, **89**, 523–542.

30 W. Ben Nasr, K. Karoui, A. Bulou and A. Ben Rhaiem, $Li_{1.5}Rb_{0.5}MoO_4$: Ferroelectric properties and characterization of phase transitions by Raman spectroscopy, *Phys. E*, 2017, **93**, 339–344.

31 K. Uchino and S. Nomura, Critical Exponents of the Dielectric Constants in Diffused-Phase-Transition Crystals, *Ferroelectr., Lett. Sect.*, 1982, **1**, 55–61.

32 D. Viehland, M. Wuttig and L. E. Cross, The glassy behavior of relaxor ferroelectrics, *Ferroelectrics*, 2011, **120**, 71–77.

33 T. Yan-Qing, Y. Yuan, H. Yong-Mei, D. Su-Ying and Y. Yi-Wen, Structure and dielectric properties of $Ba_5NdCu_{1.5}Nb_{8.5}O_{30}$-δ tungsten bronze ceramics, *Mater. Res. Bull.*, 2013, **48**, 1934–1938.

34 J. Tarasiewicz, R. Jakubas and J. Baran, Raman studies of the anionic sublattices vibrations in $(C_5H_5NH)_6Bi_4Cl_{18}$, *J. Mol. Struct.*, 2002, **614**, 333–338.

35 P. d. R. Andrade and S. P. S. Porto, Hard core phonon frequency at transition temperature, *Solid State Commun.*, 1974, **14**, 547–550.

36 T. S. Jung, H. L. Liu and J. T. Yu, Raman Study of the Phase Transition in $[N(C_2H_5)_4]_2ZnCl_4$ Single Crystals, *Chin. J. Phys.*, 2001, **39**, 344–348.

37 G. Lucazeau, Effect of pressure and temperature on Raman spectra of solids: anharmonicity, *J. Raman Spectrosc.*, 2003, **34**, 478–496.

38 M. Oussaid, P. Becker and C. Carabatos-Nedelec, Raman scattering investigation of order–disorder phase transitions in cadmium tris(thiourea) sulphate (CTS), *J. Raman Spectrosc.*, 2000, **31**, 529–533.

39 N. Moutia, M. Ben Gzaiel, A. Oueslati and K. Khirouni, Electrical characterization and vibrational spectroscopic investigations of order–disorder phase transitions in $[N(C_3H_7)_4]_2CoCl_4$ compound, *J. Mol. Struct.*, 2017, **1134**, 697–705.

40 C. Carabatos-Nédelec and P. Becker, Order–disorder and structural phase transitions in solid-state materials by Raman scattering analysis, *J. Raman Spectrosc.*, 1998, **28**, 663–672.

41 P. Schiebel and W. Prandl, Single particle dynamics in an anharmonic potential with translation-rotation coupling: crossover from weak localisation *via* chaos to free rotation, *Z. Phys. B: Condens. Matter*, 1997, **104**, 137–145.

42 F. Jebari, P. Becker and C. Carabatos-Nédelec, Order–disorder phase transition in diethylenetriammonium chlorocadmate single crystals determined by Raman spectroscopy, *J. Raman Spectrosc.*, 1994, **25**, 261–265.

43 M. Oussaïd, P. Becker and C. Carabatos-Nédelec, Low Temperature Phase Transitions in Zinc Tris (Thiourea) Sulfate (ZTS) Determined by Raman Scattering, *Phys. Status Solidi B*, 1998, **207**, 103–110.

44 E. Szostak, A. Migdal-Mikuli, A. Kaczor and W. Nitek, Low-temperature phase transition in $[Mn(OS(CH_3)_2)_6](ClO_4)_2$ studied by single crystal X-ray diffraction, infrared absorption and Raman scattering spectroscopies, *Spectrochim. Acta, Part A*, 2011, **79**, 1179–1186.